THE ASTROPHYSICAL JOURNAL, 487:437–446, 1997 September 20

EVOLUTION OF ERUPTIVE FLARES. I. PLASMOID DYNAMICS IN ERUPTIVE FLARES

TETSUYA MAGARA,[1] KAZUNARI SHIBATA,[2] AND TAKAAKI YOKOYAMA[2]

Received 1996 December 31; accepted 1997 April 15

ABSTRACT

We investigate the resistive processes of plasmoid dynamics in eruptive flares by performing 2.5-dimensional resistive MHD numerical simulations. We start with a linear force-free field arcade and impose the localized resistive perturbation on the symmetry axis of the arcade. Then the magnetic fields begin to dissipate, producing inflows toward this region. These inflows make the magnetic fields convex to the symmetry axis and hence a neutral point is formed on this axis, leading to a formation of a magnetic island around the symmetry axis. At the first stage, the magnetic island slowly rises by the upflow produced by the initial resistive perturbation. Then, once the anomalous resistivity sets in, the magnetic island begins to be accelerated. This acceleration stops after the fast MHD shock is formed at the bottom of the magnetic island, which implies that the upflow around the central part of the magnetic island is no longer strong. These three stages in the evolution of the plasmoid are confirmed to exist in the observational results. Moreover, a time lag between the start time when the magnetic island begins to be accelerated and the peak time of the neutral-point electric field can be explained by the inhibition of magnetic reconnection by the perpendicular magnetic field. We also study the difference of the initial rise motion of the plasmoid between the simulation results and the observational ones, and we conclude that, in actual situations, the initial resistive perturbation proceeds very weakly and at many positions inside the arcade.

Subject headings: MHD — Sun: corona — Sun: flares — Sun: magnetic fields

1. INTRODUCTION

We can observe many activities in the outer atmosphere of the Sun. Solar flares are one of the most popular active phenomena and hence have been so attractive to both theorists and observers that much work has been done with these objects. Solar flares are highly energetic and complicated phenomena in which mass eruptions occur, energetic particles are generated, and soft or hard X-rays are radiated. In this paper, we study the dynamics of mass eruptions associated with solar flares, which are sometimes called plasmoid eruptions or filament eruptions (observed in Hα).

Theoretically, these eruptive phenomena have been considered to be related to an instability or a loss of equilibrium of the coronal magnetic field. Since the magnetic force is much stronger than both the gas pressure and the gravity force in the corona, coronal structures are mainly controlled by the magnetic field. Therefore, unless a magnetically driven event occurs, the coronal structures evolve in a series of quasi-static states, but once an instability develops or a loss of equilibrium is achieved, they no longer stay in a static state and enter on a dynamical stage. This scenario has made it important to study the stabilities and natures of the equilibrium configurations of the coronal magnetic field. Zweibel (1981, 1982) investigated the stabilities of two-dimensional magnetohydrostatic configurations. Cargill, Hood, & Migliuolo (1986), Velli & Hood (1986), and Hood & Anzer (1987) studied the MHD stabilities of the cylindrically symmetric magnetic arcades. Viscous effect was discussed by van der Linden, Goossens, & Hood (1988) and Bogaert & Goossens (1991). Zwingmann (1987) showed a series of equilibria of the coronal magnetic field and explained the onset conditions for the eruptive phenomena, which were reconsidered by Platt & Neukirch (1994). Priest (1988) and Steele et al. (1989) discussed a loss of equilibrium from the viewpoint of CME (coronal mass ejection). Forbes, Priest, & Isenberg (1994) estimated the amount of released energy when a loss of equilibrium occurs. An approach to this kind of problem by using the complex analyses is found in Priest & Forbes (1990) and Forbes (1990), for example.

Recently, the rapid development of computers enabled us to trace the temporal evolution of the coronal magnetic field directly by means of numerical simulations. Such work is found in Mikic, Barnes, & Schnack (1988), Biskamp & Welter (1989), Finn, Guzdar, & Chen (1992), Inhester, Birn, & Hesse (1992), Kusano, Suzuki, & Nishikawa (1995), Choe & Lee (1996), for example. These papers studied how the coronal magnetic field evolved under those situations where the shearing or converging motion was imposed in the photosphere.

Turning to the observations, the satellite *Yohkoh* has brought us many intriguing data of the corona since its launch in 1991 August (Masuda 1994; Sakao 1994; Hara 1996). These data are of good quality, so that they can be used to confirm the preproposed theories of several solar phenomena, for example, the reconnection model of solar flares (Tsuneta et al. 1992; Magara et al. 1996), as well as to propose some new theoretical predictions (Shibata et al. 1994, 1995). As for the plasmoid eruptions, Ohyama & Shibata (1997) analyzed the time-varying behavior of the plasmoids in detail and clarified their dynamical natures. The aim of our paper is to understand theoretically what is the basic mechanism working in the plasmoid eruption by taking into account some new results obtained by *Yohkoh*. For this purpose, we perform 2.5-dimensional resistive MHD simulations and compare the simulation results with the observational ones.

Basic formulations are in the next section. Main results are presented in § 3, and § 4 is used to mention the observational results. In § 5 we discuss both the obtained results

[1] Department of Astronomy, Faculty of Science, Kyoto University, Sakyo-ku, Kyoto 606-01, Japan; magara@kusastro.kyoto-u.ac.jp.
[2] National Astronomical Observatory, Mitaka, Tokyo 181, Japan.

and the related problems and give our conclusions. The final section is devoted to summary.

2. BASIC FORMULATIONS

2.1. *Basic Equations*

We consider the magnetized atmosphere composed of both the magnetic field and the ideal gas. The effect of the gravity is neglected for simplicity. Using the Cartesian coordinates, the basic equations are

$$\frac{\partial \rho}{\partial t} + \nabla \cdot (\rho \boldsymbol{v}) = 0 , \tag{1}$$

$$\rho\left[\frac{\partial \boldsymbol{v}}{\partial t} + (\boldsymbol{v} \cdot \nabla)\boldsymbol{v}\right] = -\nabla P + \frac{1}{4\pi}(\nabla \times \boldsymbol{B}) \times \boldsymbol{B} , \tag{2}$$

$$\frac{\rho^{\gamma}}{\gamma - 1}\left[\frac{\partial}{\partial t}\left(\frac{P}{\rho^{\gamma}}\right) + (\boldsymbol{v} \cdot \nabla)\left(\frac{P}{\rho^{\gamma}}\right)\right] = \frac{\eta}{4\pi}|\nabla \times \boldsymbol{B}|^2 , \tag{3}$$

$$\frac{\partial \boldsymbol{B}}{\partial t} = \nabla \times (\boldsymbol{v} \times \boldsymbol{B}) - \nabla \times (\eta \nabla \times \boldsymbol{B}) , \tag{4}$$

$$P = \frac{\rho R T}{\mu} . \tag{5}$$

In addition, we use $\nabla \cdot \boldsymbol{B} = 0$ as an initial condition for equation (4). Here all the symbols, such as P, ρ, T, $\boldsymbol{v}$, and $\boldsymbol{B}$, have their usual meanings, γ is the adiabatic index, R is the gas constant, μ is the mean molecular weight, and η is the magnetic diffusivity. All physical values are dependent on both the x and z coordinates, but constant along the y-coordinate. In practice, calculations are performed for the nondimensional values normalized by some particular units. These units are summarized in Table 1.

2.2. *Initial Configuration*

Initially we assume a linear force-free field described by

$$B_x = -\frac{2L}{\pi H} B_0 \cos\left(\frac{\pi}{2L} x\right) e^{-z/H} , \tag{6}$$

$$B_y = -\sqrt{1 - \left(\frac{2L}{\pi H}\right)^2} B_0 \cos\left(\frac{\pi}{2L} x\right) e^{-z/H} , \tag{7}$$

$$B_z = B_0 \sin\left(\frac{\pi}{2L} x\right) e^{-z/H} , \tag{8}$$

where L is the horizontal scale length and is taken as the normalized length unit ($L = 1.0$); H means the vertical scale height of the magnetic field. For the present study, H ranges from $2L/\pi$ to ∞, where $H = 2L/\pi$ corresponds to the potential field and $H = \infty$ corresponds to the open field. Usually, a linear force-free field is characterized by a constant parameter α, where

$$\nabla \times \boldsymbol{B} = \alpha \boldsymbol{B} , \tag{9}$$

and this value is described by $\alpha = [(\pi/2L)^2 - (1/H)^2]^{1/2}$ in our formulation. Therefore, α ranges from 0 (potential field) to $\pi/2L$ (open field). A linear force-free field is the lowest energy state for the given boundary conditions with prescribed helicity (see Heyvaerts & Priest 1984), but in reality the coronal magnetic field is not always considered to be in this state (Schmieder et al. 1996). This is because the relaxation time to this state is not so short as the dynamical time (see Browning & Priest 1986). However, in the present study we start with this state for simplicity.

The gas pressure P is uniform ($P = P_0$), and the ratio of this to the magnetic pressure is defined as $\beta \equiv 8\pi P_0/B^2$ (plasma β). The gas density ρ is uniform ($\rho = \rho_0$) except in the bottom region where it is 10 times higher than elsewhere. This region is modeled on the massive layers of the solar atmosphere, such as the chromosphere and the photosphere. Therefore, the gas pressure and density are expressed by

$$P = P_0 , \tag{10}$$

$$\frac{\rho}{\rho_0} = 4.5\{\tanh[-50(z - 0.1)] + 1\} + 1 , \tag{11}$$

respectively. Plasma β is also expressed by

$$\beta = \frac{P_0}{(B^2/8\pi)} = \frac{P_0}{(B_0^2/8\pi)e^{-(2z/H)}} = \beta_0 e^{(2z/H)} . \tag{12}$$

In the present study, we adopt $\beta_0 = 0.2$, $\gamma = 5/3$, $P_0 = 1/\gamma$, $\rho_0 = 1$, and $B_0 = (8\pi P_0/\beta_0)^{1/2} = (8\pi/\gamma\beta_0)^{1/2}$. From now on, all physical values presented in this paper are normalized by the units in Table 1.

Finally, the temperature is defined by

$$T = \gamma \frac{P}{\rho} , \tag{13}$$

in the nondimensional form.

TABLE 1

UNITS FOR NORMALIZATION

Physical Values	Normalization Units	Typical Values
Length	L[a]	5000 (km)
Velocity	C_{s0}[b]	300 (km s^{-1})
Time	L/C_{s0}	20 (s)
Density	ρ_0	10^{-14} (g cm^{-3})
Pressure	$\rho_0 C_{s0}^2$	10 (dyne cm^{-2})
Temperature	$\mu C_{s0}^2/\gamma R$	3×10^6 (K)
Magnetic Field	$(8\pi\rho_0 C_{s0}^2/\gamma\beta_0)^{1/2}$	8×10^2 (G)
Electric Field	$C_{s0}(8\pi\rho_0 C_{s0}^2/\gamma\beta_0)^{1/2}/c$	2×10^4 (V m^{-1})
Magnetic Diffusivity	$C_{s0} L$	5×10^{16} (cm^2 s^{-1})

NOTE.—The parameters ρ_0, T_0, and C_{s0} are taken to be the coronal values in the active region. γ, μ, β_0, R, and c are the adiabatic index, the mean molecular weight, the plasma beta, the gas constant, and the speed of light, respectively.

[a] L is a half-length between the footpoints of a loop.

[b] C_{s0} is the adiabatic sound velocity defined by $C_{s0} \equiv (\gamma R T_0/\mu)^{1/2}$.

2.3. *Boundary Conditions*

Figure 1 illustrates the domain of the present numerical simulation. This figure also shows the initial configuration of the magnetic field lines projected onto the (x, z) plane. We set a free boundary condition at the upper boundary (at $z = 40$),

$$\frac{\partial B_x}{\partial z} = \frac{\partial B_y}{\partial z} = \frac{\partial v_x}{\partial z} = \frac{\partial v_y}{\partial z} = \frac{\partial v_z}{\partial z} = \frac{\partial P}{\partial z} = 0 , \quad \nabla \cdot \boldsymbol{B} = 0 , \tag{14}$$

and antisymmetric boundary conditions both along the z-axis (at $x = 0$) and along the side boundary (at $x = 8$),

$$v_x = v_y = B_z = \frac{\partial v_z}{\partial x} = \frac{\partial B_x}{\partial x} = \frac{\partial B_y}{\partial x} = \frac{\partial P}{\partial x} = \frac{\partial \rho}{\partial x} = 0 , \tag{15}$$

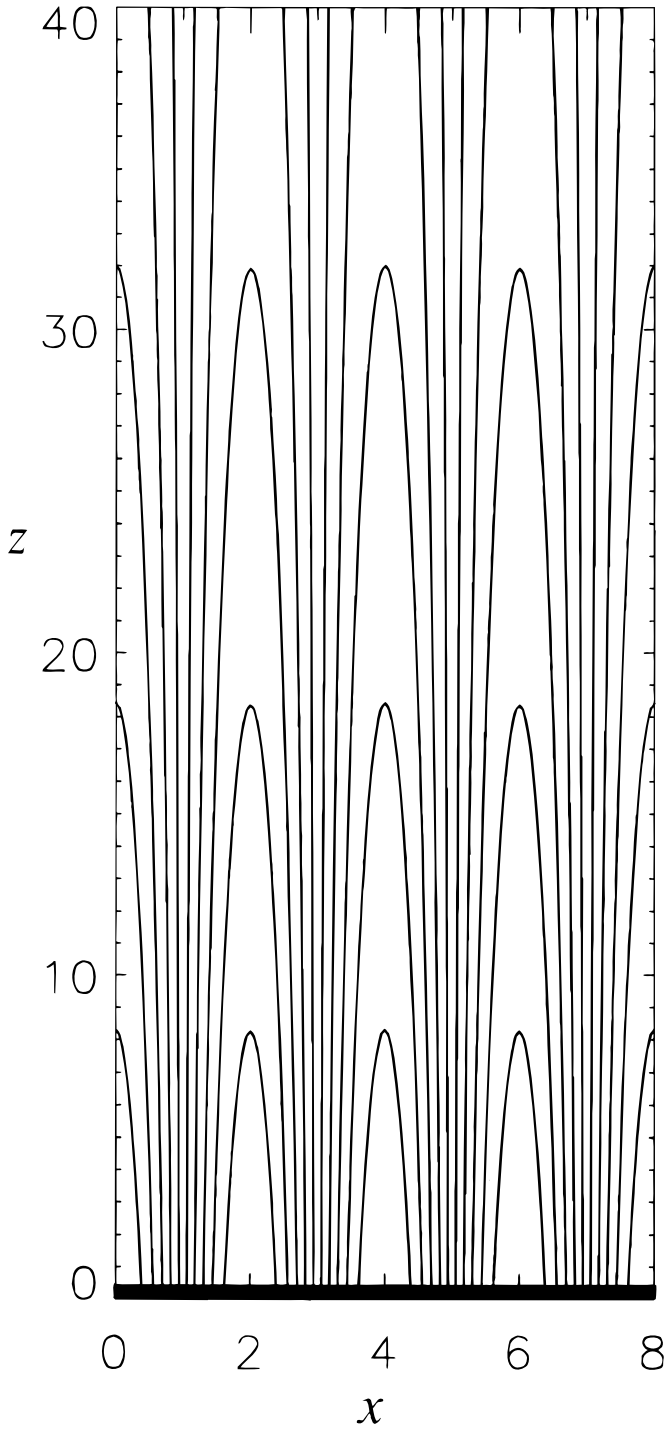

FIG. 1.—Initial configuration of the present numerical simulation. Contours indicate magnetic field lines projected onto the (x, z) planes. The dark region at the bottom is a high-density region modeled on the massive atmosphere, such as the chromosphere and the photosphere.

and a rigid boundary condition for the lower boundary (at $z = 0$),

$$v_y = v_z = \frac{\partial v_x}{\partial z} = \frac{\partial B_x}{\partial z} = \frac{\partial B_y}{\partial z} = \frac{\partial B_z}{\partial z} = \frac{\partial P}{\partial z} = \frac{\partial \rho}{\partial z} = 0 , \quad (16)$$

respectively. For the actual calculations, we use the modified Lax-Wendroff method developed by Shibata and Yokoyama (see Shibata et al. 1989; Yokoyama 1995) and solve the equations only over a half domain ($0 \le x \le 8$), assuming a symmetry at $x = 0$. The numbers of the mesh points are $(N_x \times N_z) = (160 \times 200)$, where the mesh points are distributed uniformly in both of the x and z directions and hence the grid size is $(\Delta x, \Delta z) = (0.05, 0.2)$.

Although multiple arcades exist in the calculated region, our attention is concentrated only on the central one ($0 \le x \le 1$). The other ones are set in order to make a smooth boundary condition at $x = 1$. That is, if we set the free boundary condition at $x = 1$, the effect of the resultant numerical flows would not be negligible. From this point of view, the initial perturbations are assigned to the central arcade alone (see below), and we investigate this arcade's evolution.

2.4. *Initial Perturbations*

Initially, the diffusivity coefficient is set to be $\eta = 0$ everywhere, except in a narrow region of $[x^2 + (z - h)^2]^{1/2} \le r$, in which $\eta = \eta_{\rm init}$ is assigned for a finite time ($0 \le t \le 2$). Here η is the normalized value and defined as the reciprocal of the modified magnetic Reynolds number R_m ($\equiv C_s L/\eta$). Values h and r are those parameters which determine the height and radius of the initially perturbed region. In the present study, we take various models having different values of such parameters as $\eta_{\rm init}$, h, and r. These models are summarized in Table 2. As far as the radius r is concerned, all models have $r \le 0.9$, which is because we focus our concentration on the central arcade. Model r1–r4 and model $\eta 1$–$\eta 3$ are characterized by the radius r and initially assigned resistivity $\eta_{\rm init}$, respectively. These models are used in order to investigate how the natures of the initially perturbed region affect the subsequent evolution of the system (see § 3.3). Model H1–H4 are different with each other in their vertical scale heights. Model M, unlike those models mentioned above, has four distinct initially perturbed regions rather than a single perturbed region, which are all distributed along the z-axis.

After a finite value of resistivity ($\eta_{\rm init}$) is assigned in the perturbed region, the magnetic fields begin to dissipate, causing inflows toward this region. These inflows make the magnetic fields convex to the symmetry axis ($x = 0$) and hence a neutral point is formed on this axis. Then, not only the current density increases in this neutral point but also the gas density around this point decreases because the matter here is ejected away by the outflow, which eventually turns on the anomalous resistivity. This anomalous resistivity is considered to be one of the most important factors among several physical processes capable of causing the fast magnetic reconnection. The anomalous resistivity is known to have a close relationship with the plasma microturbulence. Suppose that the spacial variation of the magnetic field is so steep and the gas density is so low that the ion-electron drift velocity can exceed the ion's thermal velocity, the plasma microturbulence is excited, providing a seed for the anomalous resistivity (see Parker 1979, 1994; Bermann, Tetreault, & Dupree 1985). Yokoyama & Shibata (1994) studied the conditions of the fast magnetic reconnection and found that the anomalous resistivity played an essential role in this process. Ugai pointed out the essence of this fast magnetic reconnection by "the spontaneous fast reconnection model," which describes a (new-type) nonlinear instability that grows by the self-consistent interaction (feedback) between (microscopic) anomalous resistivities and (macroscopic) global reconnection flows (Ugai 1996).

TABLE 2

MODEL DESCRIPTION

	MODELS											
	r Dependence				η Dependence			H Dependence				MULTI-RESISTIVE REGION
PARAMETER	r1	r2	r3	r4	η1	η2	η3	H1	H2	H3	H4	M
r[a]	0.3	0.5	0.7	0.9	0.7	0.7	0.7	0.5	0.5	0.5	0.5	0.7
η_{init}[b]	1/15	1/15	1/15	1/15	1/20	1/30	1/60	1/30	1/30	1/30	1/30	1/15
v_c[c]	50	50	50	50	50	50	50	—	—	—	—	50
h[d]	5	5	5	5	5	5	5	5	5	5	5	5, 10, 15, 20
H[e]	40	40	40	40	40	40	40	40	20	10	5	40

[a] r is the radius of the initially perturbed region.
[b] η_{init} is the value of the magnetic diffusivity assigned as the initial perturbation.
[c] v_c is the threshold value of anomalous resistivity (see eq. [17]).
[d] h is the height of the initially perturbed region.
[e] H is the vertical scale height of the initial magnetic field configuration.

The anomalous resistivity is also used to understand other active phenomena in the universe. For example, Borovsky (1986) explained the extragalactic jets by hybrid double layer/anomalous resistivity model. In the present study, we assume the following form for the anomalous resistivity:

$$\eta = \begin{cases} \dfrac{1}{150}\left(\left|\dfrac{v_d}{v_c}\right| - 1\right) & \text{for } |v_d| \equiv \left|\dfrac{j_y}{\rho}\right| \geq |v_c|\,, \\ 0 & \text{for } |v_d| < |v_c|\,, \end{cases} \quad (17)$$

unless η exceeds 1. In that case η is fixed to 1. Here $\boldsymbol{j} = \nabla \times \boldsymbol{B}$, v_d is used as a relative ion-electron drift velocity, and v_c is the threshold velocity (see Ugai 1986; Yokoyama 1995). The values of v_c used in this simulation can be seen in Table 2.

3. MAIN RESULTS

3.1. *Overviews*

First, we show some typical characteristics of the evolution of eruptive flares by using the results of model r3. In Figures 2*a*–2*c* (Plate 5), we display the temporal variations of the y-component of the magnetic field (hereafter this is called the perpendicular field), the temperature, and the density, respectively. Contours represent the magnetic field lines projected onto the (x, z) planes, and arrows represent the fluid velocity fields on the same planes. The region of $0 \leq z \leq 30$ is the only one displayed since we take into account the limitation from neglecting the gravity effect. According to Tsuneta (1996), the temperature of the active region in the corona is typically 2–4 MK for the background component of the corona. If we take 3 MK for its temperature, the pressure scale height is about $50T = 1.5 \times 10^8$ m (see Priest 1982), which is 30 times longer than a half-length between the footpoint of a loop (5000 km is assumed; see Table 1). Therefore, a reasonable vertical extent of the system under the assumption of neglecting the gravity effect is at most $0 \leq z \leq 30$. In addition, we can avoid the problem of the numerical flows born in the upper free boundary ($z = 40$) by setting the tentative upper boundary far from this upper free boundary.

From these figures, we can find that the magnetic island is formed and rising upward with time. In Figure 2*b*, both at the bottom of the upper magnetic island and at the top of the lower closed loop very hot regions are formed ($t = 12.0$). As for the density map (Fig. 2*c*), the high-density region of the Y shape is found to be appearing at the bottom of the magnetic island ($t = 12.0$).

Figure 3 shows the temporal variations of both the y-component of the electric field (E_y) at the neutral point (X-point) and the height of the magnetic island of model r3, which are represented by the thin solid line and crosses, respectively. The height of the magnetic island is defined by measuring the height of the O-point, where B_x changes its sign inside the magnetic island. Thick solid lines represent the results of the line fitting for this temporal variation of the height of the magnetic island. The time ranges for these two line fittings are $0 \leq t \leq 5$ for the first and $15 \leq t \leq 17$ for the second, respectively. These time ranges are defined by the temporal behavior of the neutral-point electric field; the first time range corresponds to when this electric field does not arise and the second corresponds to when this electric field rapidly decreases.

This figure indicates that after the initially perturbed phase ($0 \leq t \leq 2$), the anomalous resistivity is turned on at $t = 5$, which gives rise to the neutral-point electric field. This is because the neutral-point electric field is proportional to the reconnection rate at this point (see Forbes & Priest 1983). This electric field reaches its maximum at $t = 14$

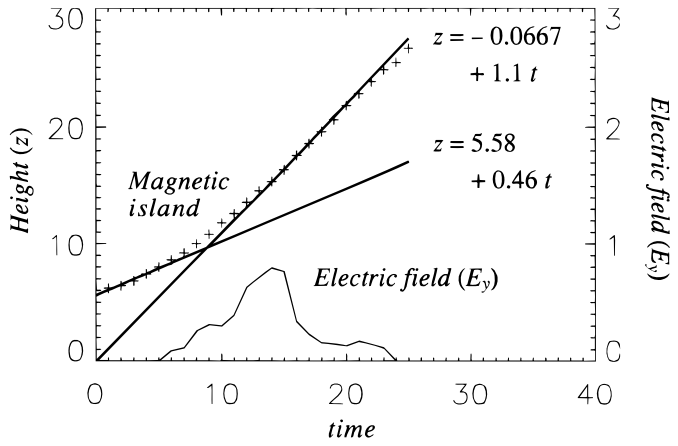

FIG. 3.—Temporal variations of both y-component of electric field (E_y) at the neutral point (X-point) and height of magnetic island of model r3, which are represented by thin solid line and crosses, respectively. Thick solid lines represent the results of line fitting for this temporal variation of height of magnetic island. (Each time range for the line fitting is $0 \leq t \leq 5$ for the first and $15 \leq t \leq 17$ for the second, respectively.)

when the anomalous resistivity is large, and then rapidly decreases, which is due to the loss of the magnetic field inflowing toward the neutral point. As for the dynamics of the magnetic island, the magnetic island is slowly going upward initially ($0 \leq t \leq 5$), then is accelerated during $5 \leq t \leq 12$, and finally has a constant rise velocity ($12 \leq t$). In order to clarify what kind of mechanism plays an important role at each three stages, we pick three distinct times ($t = 3$, 6, and 12) and investigate the physical situations for these times, which correspond to the times when the magnetic island is slowly rising, begins to be accelerated, and has a constant rise velocity, respectively.

Figures 4*a*, 4*b*, and 4*c* shows the distributions along the z-axis of the perpendicular field (B_y), the vertical velocity (v_z), and the neutral-point electric field (E_y) at $t = 3$, 6, and 12, respectively. B_y, v_z, and E_y are represented by the thin dotted lines, solid lines, and broken lines, respectively. The positions of the O-point are also represented by the vertical thick solid lines in all these figures.

At $t = 3$ (Fig. 4*a*), E_y is 0 because the anomalous resistivity does not start yet. Looking at the position of the O-point, we find that the magnetic island rises upward slowly, moving in the upflow produced by the initial perturbation. As this process proceeds, the matter around the neutral point is ejected away and hence the gas density around the neutral point decreases, leading to the start of the anomalous resistivity ($t = 5$). This effect increases the upflow velocity so that the magnetic island begins to be accelerated. At $t = 6$ (Fig. 4*b*), we find that the upward velocity at the O-point is about 1.5 times higher than at $t = 3$ (Fig. 4*a*). Although the start time of the acceleration of the magnetic island corresponds to the occurrence time of the anomalous resistivity, the electric field at the neutral point does not take its maximum value at that time, when a large amount of perpendicular magnetic field (B_y) still exists around the neutral point (see Fig. 4*b*). According to the experimental research, the rate of the magnetic reconnection with the perpendicular field is lower than without it (Ono, Morita, & Katsurai 1993). When the perpendicular field is lost around the neutral point, then the rate of the magnetic reconnection becomes so high that the neutral-point electric field also has high value. This process can be confirmed in Figure 4*c* ($t = 12.0$). At this stage, the upflow has a very high speed (reconnection jet) because of the efficient magnetic reconnection so that it forms the fast MHD shock at the bottom of the magnetic island. (The position of this shock is shown in Fig. 4*c* by the vertical thick broken line.) It is found that the O-point is behind this shock, and therefore the magnetic island is no longer accelerated efficiently, leading to having a constant rise velocity. (Such behavior of the perpendicular field described above is also seen in Fig. 2*a*. At $t = 12.0$, the region around the neutral point ($z \sim 5$) is colored in white, which means that the amount of perpendicular field is little in this region.)

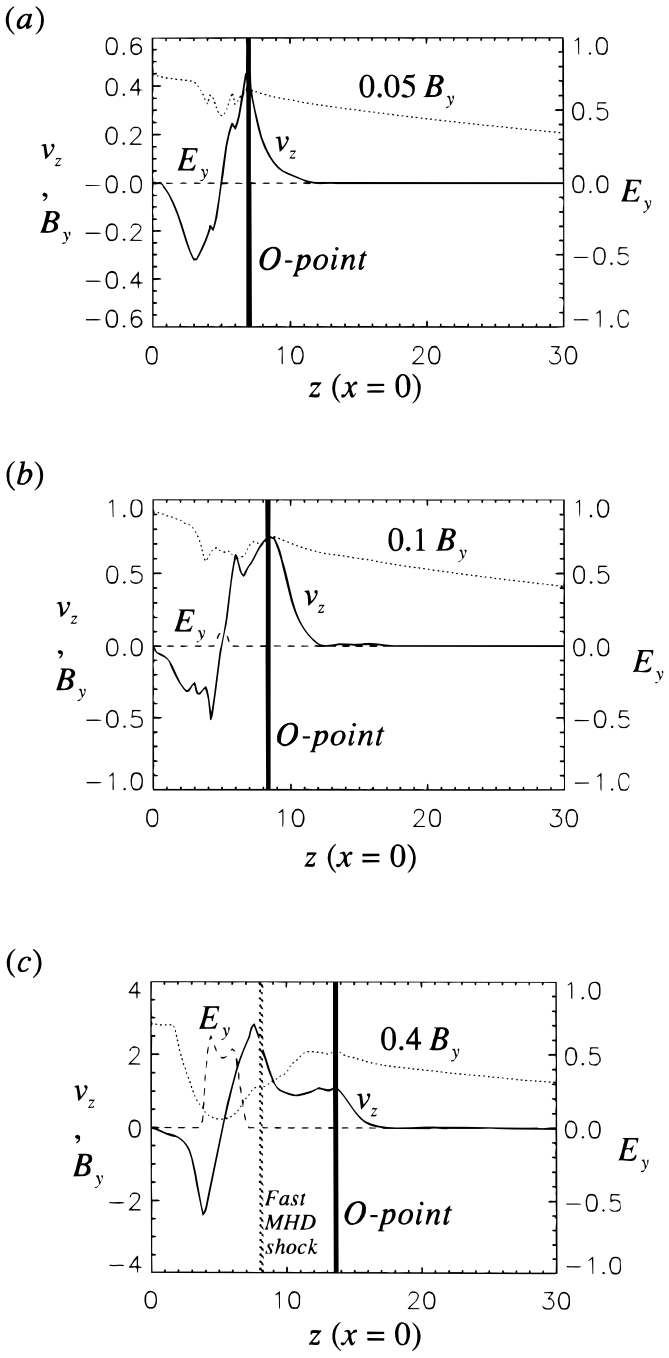

FIG. 4.—Distributions along the z-axis of perpendicular field (B_y), vertical velocity (v_z), and neutral-point electric field (E_y) at (*a*) $t = 3$, (*b*) 6, and (*c*) 12, respectively. B_y, v_z, and E_y are represented by thin dotted lines, solid lines, and broken lines, respectively. Positions of O-point are represented by vertical thick solid lines in all these figures. In (*c*), position of fast MHD shock is also shown by vertical thick broken line.

3.2. *Parameter Dependences*

Following the results of § 3.1, where we show some characteristics of the evolution of eruptive flares, we question whether these characteristics are common or not, that is, how the nature of the initial perturbations affects these evolutions. To investigate this, we take those models in which we not only vary the radius r of the initially perturbed region (models r1–r4) and the magnitude of the initially assigned magnetic diffusivity $\eta_{\rm init}$ (models η1–η3), but also assign the initial perturbation not at a single position but at four different positions (model M). Then, for all these models we make those plots similar to Figure 3 and compare their features. As a consequence, we find that there are some similarities among these features, such as the three stages in the dynamical evolution of the magnetic island and the time lag between the start time of the magnetic island acceleration and the peak time of the neutral-point electric field. However, we find two characteristics fairly changed. One of them is the upward velocity of the mag-

netic island, and the other is the coalescence process of the multiple magnetic islands.

Figures 5*a* and 5*b* indicate the variations of the upward velocity of the magnetic island with r and $\eta_{\rm init}$, respectively. Here the upward velocities are derived from the inclinations obtained by those line fittings in all models (models r1–r4, η1–η3) similar to Figure 3. In both figures asterisks and crosses represent the upward velocities at the first stage (before the acceleration) and the third stage (after the acceleration), respectively. Thick curves are the results of such curve fittings as $v_{\rm upward} = ar^b$ and $c\eta_{\rm init}^d$, where a, b, c, and d are all constant. When $r = 0$ or $\eta_{\rm init} = 0$, we obtain $v_{\rm upward} = 0$, which means there is no initial perturbation.

These figures tell us that the upward velocities at both the first and the third stages decrease as the initial perturbation becomes weak (in a sense of r and $\eta_{\rm init} \to 0$). Moreover, there is a difference in a manner of decrease between both stages. Looking at the powers in the results of the curve fittings, the decrease at the third stage is gentler than at the first stage.

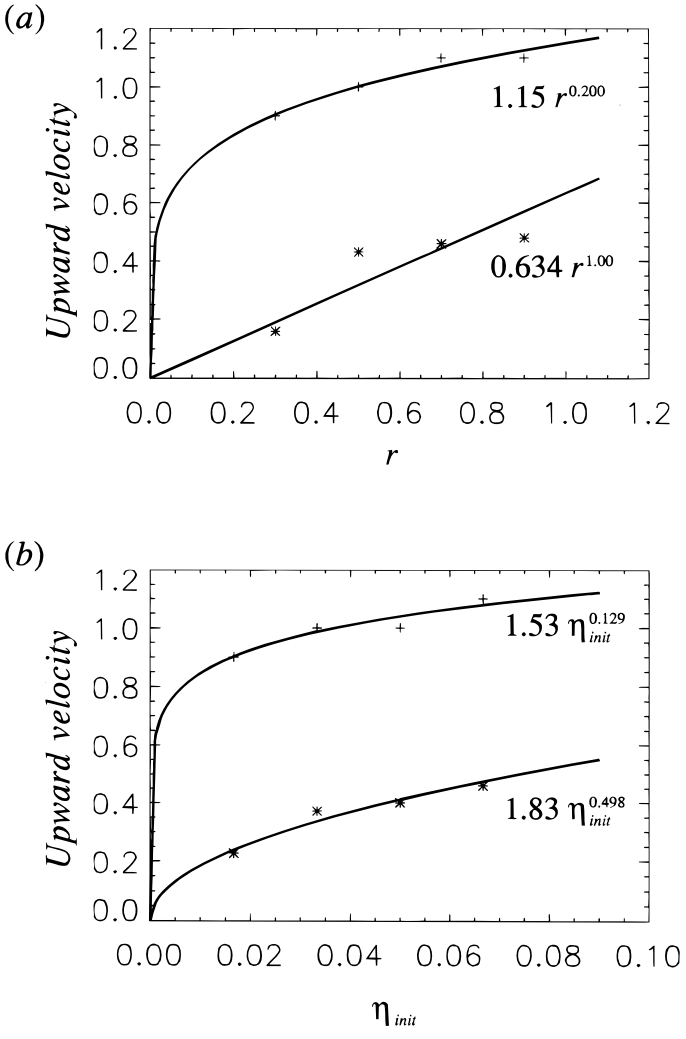

FIG. 5.—Variations of upward velocity of magnetic island with (*a*) r (models r1–r4) and (*b*) $\eta_{\rm init}$ (models η1–3 and r3), respectively. Upward velocities are derived from the inclinations obtained by line fittings for temporal variations of height of magnetic island in each model similar to Fig. 3. In both figures asterisks and crosses represent upward velocities at the first stage (before acceleration) and the third stage (after acceleration), respectively. Thick curves are the results of such curve fittings as $v_{\rm upward} = ar^b$ and $c\eta_{\rm init}^d$, where a, b, c, and d are all constant.

This difference can be considered to reflect the each stage's sensitivity to the initial perturbation; the upward velocity at the first stage is directly connected with the initial perturbation, while the upward velocity at the third stage is under the circumstance in which the anomalous resistivity already arises so that the effect of the initial perturbation on this stage is relatively weak.

Figure 6*a* (Plate 6) shows the evolution of model M. Top and bottom panels are the temperature and density maps, respectively. Contours represent the magnetic field lines projected onto the (x, z) planes, and arrows represent the fluid velocity fields on the same planes. At $t = 5.0$ we can find four X-points (z = 5, 10, 15, and 20), which correspond to the initially perturbed positions. Figure 6*b* shows this model's temporal variations of both the height of every four magnetic island and the neutral-point electric field at the lowest X-point ($z = 5$) which always has a higher value than any other X-points (z = 10, 15, and 20). Crosses, asterisks, dots, and diamonds represent the height of every magnetic island, while the thin solid line shows the temporal variation of the neutral-point electric field at the lowest X-point. The temporal variation of the height of the lowest magnetic island is line-fitted in the same way as in Figure 3, and the results are represented by two thick solid lines.

From Figure 6*a*, it can be seen that the lowest magnetic island continues to merge the other upper islands except the highest one with time. At $t = 20$, there appears a well-developed magnetic island between $z = 10$ and $z = 20$, at the bottom of which a hot and dense region is formed. This configuration is quite similar to the one at $t = 12$ in Figure 2*b* and 2*c*. Referring to Figure 6*b*, we can find that the coalescence process occurs, and there are some similar features to what are recognized in the single perturbed region models described above, such as the existence of three stages in the dynamical evolution of the magnetic island and the time lag between the start time of the magnetic island acceleration and the peak time of the neutral-point electric field.

On the basis of those results shown above, we consider that those two features—the existence of three stages in the dynamical evolution of the magnetic island and the time lag between the start time of the magnetic island acceleration and the peak time of the neutral-point electric field—are important factors in understanding the evolution of plasmoid eruptions. In § 5, we discuss them in detail, but before

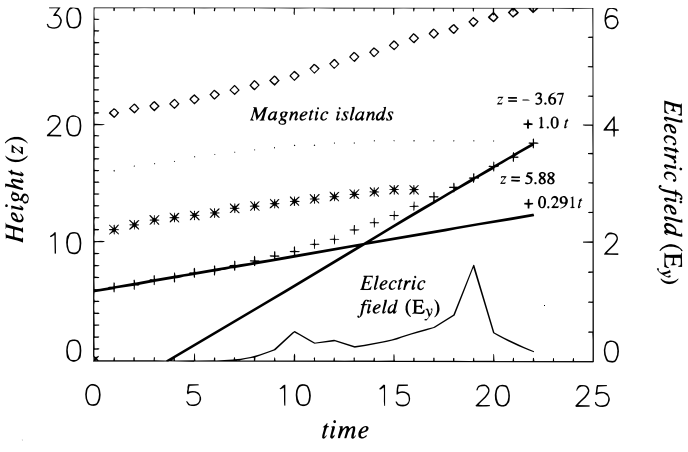

FIG. 6*b*

doing that, several observational results related to this subject are described briefly in the next section.

4. OBSERVATIONAL RESULTS

In this section, we show some observational data obtained by *Yohkoh*, which help us to understand mass eruptions associated with solar flares. In addition, we exhibit one of the interesting results of plasmoid eruptions, which were originally analyzed by Ohyama & Shibata (1997), and make some comments.

Figure 7*a* (Plate 7) shows the evolution of the eruptive processes in a typical long-duration flare (Tsuneta et al. 1992; Hudson 1994) observed by *Yohkoh*. White arrows indicate an erupted mass (plasmoid). Figure 7*b* shows the GOES X-rays plot at the same time.

These figures clearly show the apparent features of the eruptive flare evolving from the preflare phase to the rise phase. The bottom right panel in Figure 7*a*, which corresponds to the rise phase (see Fig. 7*b*), shows a mass of the Y-shape is ejecting upward. This shape is quite similar to the hot and dense region formed at the bottom of the magnetic island which is shown in Figures 2*b* and 2*c*, or Figure 6*a*.

Figure 8 (Ohyama & Shibata 1997) indicates the temporal variations both of the height of the plasmoid and of the hard X-ray intensity. Core and top represent the positions both of the highest and of the $1/e$ of the highest soft X-ray intensities within the plasmoid, respectively.

This figure tells us some important facts. One of them is that the plasmoid evolves in a series of several distinct stages; that is, it rises slowly from 11:04 to 11:15, then it is accelerated in a relatively short time (from 11:15 to 11:18), and finally it rises at almost constant velocity (after 11:18). Moreover, the start time of the acceleration of the plasmoid (11:15) is certainly before the peak time of the hard X-ray intensities (11:18). These features are consistent with those derived from our numerical simulations. (In this comparison, we assume that the variation of the neutral-point electric field is equal to that of the hard X-ray intensity. This assumption rests on the grounds that the observed hard X-ray is generated by the high-energy electrons accelerated by the neutral-point electric field, although the precise mechanism of this acceleration is still not fully understood.)

5. DISCUSSION

In this section we compare the simulation results with the observational ones, consider a related problem, discuss the limitations of the present study, and finally give our conclusions.

5.1. *Comparison with the Observational Results*

When we compare the simulation results with the observational ones, we find that the evolution of the magnetic island in the former is quite similar to the evolution of the plasmoid in the latter. Figures 3 and 8 show that both the magnetic island and the plasmoid have three distinct stages in their evolution, that is, the slowly rising stage, the acceleration stage, and the constant rise velocity stage. This constant rise velocity at the final stage is consistent with the results of Steele & Priest (1989), who studied the eruption of

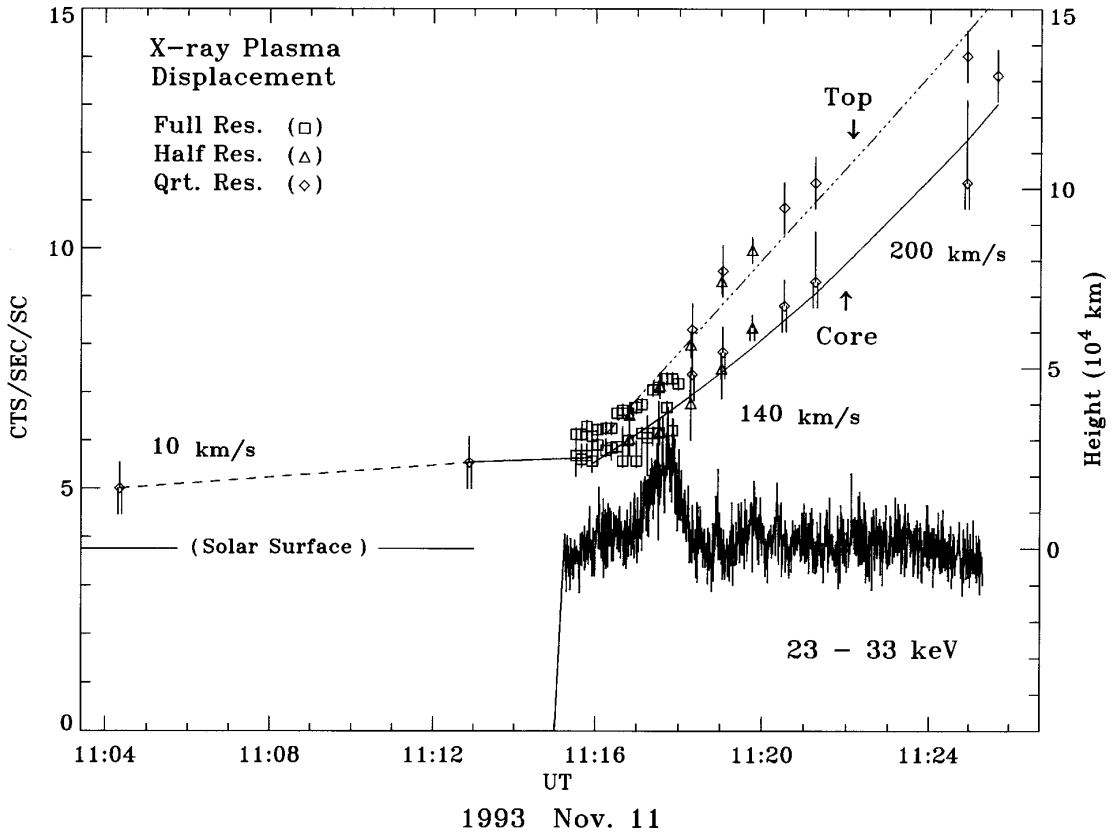

FIG. 8.—Temporal variations of the height of a plasmoid and the hard X-ray intensity in an impulsive flare on 1993 November 11 observed by the soft and hard X-ray telescopes aboard *Yohkoh* (from Ohyama & Shibata 1997). Core and top represent the positions both of the highest and the $1/e$ of the highest soft X-ray intensities within the plasmoid, respectively. For more detailed discussion, see Ohyama & Shibata (1997).

prominence. More precisely, Figure 8 indicates that the plasmoid rises very slowly in the first stage, in which the velocity is 20 times smaller than that in the third stage. On the other hand, Figure 3 shows that the initial rise velocity of the magnetic island is only half as small than the third one. We ascribe this difference to the nature of the initial perturbations. From Figures 5*a* and 5*b*, as long as the anomalous resistivity occurs, the weaker the initial perturbation is, the smaller the initial rise velocity is, without changing the final rise velocity. Therefore, one possibility is that the initial resistive perturbation proceeds very quietly in real circumstances of the corona. Another possibility is derived from Figure 6*b*. In this figure there are four magnetic islands, but the lowest one is considered to correspond to the observed plasmoid because the hot and dense region is only formed in the lowest magnetic island (see Fig. 6*a*). Although model r3 in Figure 3 and model M in Figure 6 have the same parameters of the initial perturbation ($r = 0.7$, $\eta_{\rm init} = 1/15$) except for the number of the initially perturbed regions, the initial rise velocity of model M is 60% of model r3 because the lowest magnetic island of model M is prevented from rising freely by the existence of the other upper magnetic islands. This fact that the existence of multiple islands reduces the initial rise velocity of the lowest one implies that it is more realistic for the initial perturbation to occur at many positions within an arcade.

Next, the final rise velocity is about 40% of $V_{\rm A0}$, where $V_{\rm A0} \equiv B_0/(4\pi\rho_0)^{1/2}$ and in the present study $V_{\rm A0}/C_{\rm S0} = (2/\gamma B_0)^{1/2} = 2.45$. In Magara et al. (1996), we noted that the observed ejection velocity of plasmoid was always much smaller than $V_{\rm A0}$, and hence the present result is consistent with this tendency.

5.2. *Does the Anomalous Resistivity Really Arise?*

In § 5.1 we considered the evolution of eruptive flares. There is one crucial point in those considerations, viz., the question of whether the anomalous resistivity always sets in or not. In order to answer this question, we perform those numerical simulations in which we do not assign the anomalous resistivity after the initial perturbation ($0 \le t \le 2$) and investigate the temporal variations of the parameter v_d (ion-electron drift velocity). These simulations are done with models H1–H4, which have different vertical scale heights. One result is shown in Figure 9, which shows the temporal variation of v_d at the neutral point ($v_{d,\rm neutral}$) of model H1. Here $v_{d,\rm neutral}$ is defined as the maximum value of v_d within $(0, 0) < (x, z) < (0.25, 30)$.

Figure 9 indicates that $v_{d,\rm neutral}$ is initially increasing with time and then rapidly decreasing. We think that this change is due to the effect of the finite grid size in our numerical simulation. In actual situations in the corona, it is expected that, since the plasma is continually distributed, $v_{d,\rm neutral}$ always continues to increase, and finally the microturbulences occur, causing the anomalous resistivity. Moreover, according to Schumacher & Kliem (1996), the current density at the neutral point takes larger maximum value when the Lundquist number is larger, which is suitable to the actual situations. This again suggests that the system goes over the critical point, suffering from the anomalous resistivity. From this point of view, we do curve fitting such as $v_{d0}\, e^{kt}$ for $0 < t < 8$, where v_{d0} and k are constant; this is represented by the thick solid curve.

Next, we do the same curve fittings for all the other models, models H2–H4. Then (k, H)-relation is obtained

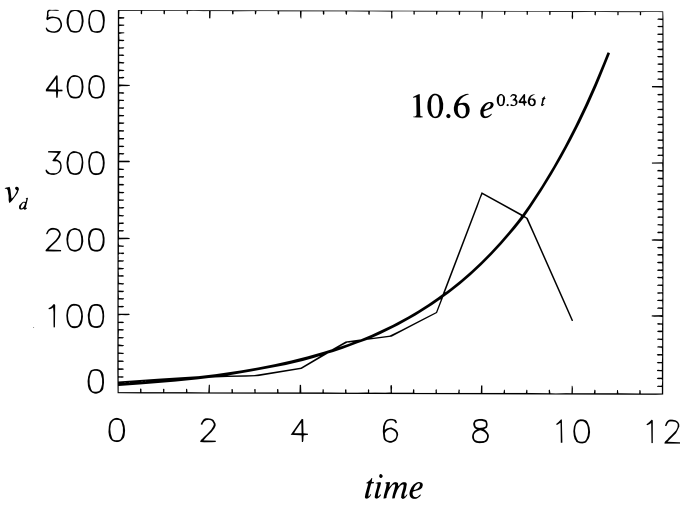

FIG. 9.—Temporal variation of v_d at the neutral point of model H1. Thick curve is the result of such curve fitting as $v_{d0}\, e^{kt}$ for $0 < t < 8$, where v_{d0} and k are constant.

and plotted in Figure 10*a*. This relation is characterized by $H = 5.53\, e^{6.05k}$, which means that (k, H) = (0, 5.5) is the limited case in which it takes an infinite time for $v_{d,\rm neutral}$ to reach its increasing phase. In Figure 10*b*, we display the same result for those models in which the height of the initially perturbed region is changed from $h = 5$ to $h = 3$. In this case the (k, H)-relation is $H = 4.55\, e^{6.79k}$. Therefore, in order to cause the anomalous resistivity, it is necessary that the vertical scale height of a magnetic arcade be several times larger than the horizontal extent of it, which is consistent with the conclusions of the bifurcation theory on solar flares in Kusano et al. (1995).

5.3. *Boundary Effect*

As we mention in § 1, direct investigations of the evolution of eruptive flares by the time-dependent numerical simulations have been often seen recently. Our work is included in this kind of work, where there has been a controversy about the effect of the boundary condition. Mikic et al. (1988) set the symmetric boundary condition at the side boundary, which was considered to have an artificial effect on the evolution by Biskamp & Welter (1989). Biskamp & Welter explained the effect of the neighboring arcades caused the eruptive phenomena by using the multiple arcade system. Instead of the effect of the neighboring arcades, van Ballegooijen & Martens (1989) and Inhester et al. (1992) considered the effect of the converging flow imposed in the photosphere. Finn et al. (1992) discussed the effect of the time-varying flow pattern for the double arcade system. In the present study, we set the antisymmetric boundary at $x = 8$, which is far enough from the boundary of the central arcade ($x = 1$) so that we can safely neglect the effect of this antisymmetric boundary at $x = 8$. However, taking the periodic arcades as an initial configuration is not suitable for simulating a single arcade in the Sun. This weak point becomes crucial at the third stage of the evolution of the magnetic island, when many magnetic fields in the neighboring arcades begin to flow into the region of the central arcade.

5.4. *Limitation of the Present Study*

As mentioned above, we use a periodic linear force-free field system in order to study the evolution of a single

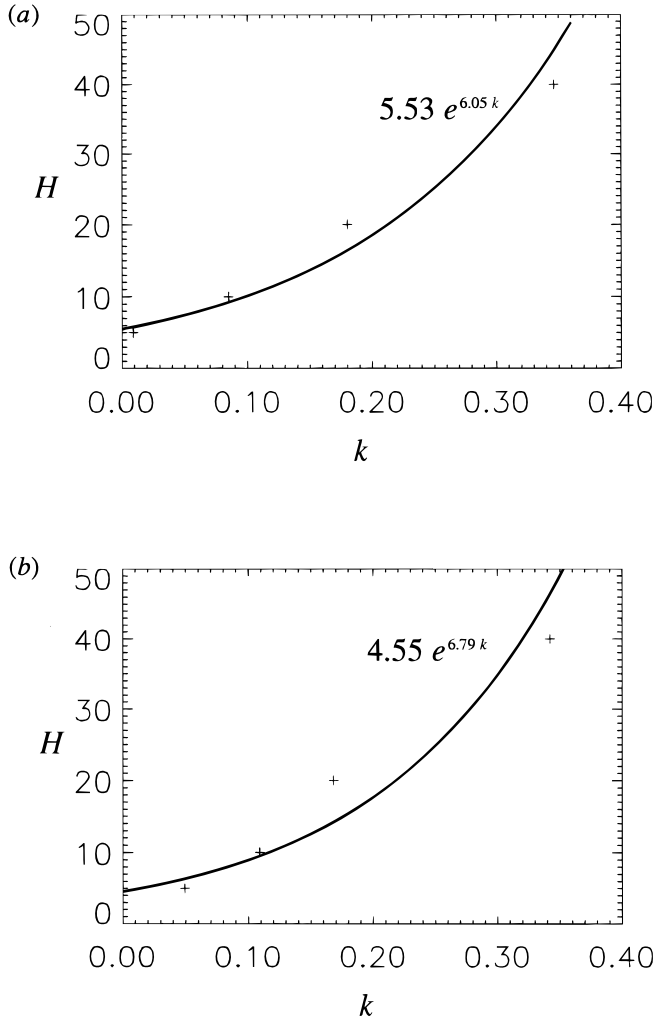

FIG. 10.—(*a*) (k, H) distribution for models H1–H4 represented by crosses. k is increasing rate of v_d, and H is vertical scale height of the magnetic field of every model. Thick curves are the results of such curve fitting as $H_0 e^{\delta k}$, where H_0 and δ are constant. (*b*) Same as (*a*), except for $h = 3$ instead of $h = 5$, where h is the height of the initially perturbed region.

arcade. This leads us to a situation in which the distribution of the magnetic field in the photosphere is assumed to be too simple, compared to the more complicated distribution of the magnetic field. This simplification brings several limitations to our present study. First, since we take only one Fourier component of the solutions to equation (9), we need a system with a large amount of magnetic energy in order to construct the highly concentrated current layer within an arcade. In actual situations, the energy within the arcade is finite; hence, we cannot estimate the amount of the released energy during a flare evolution in the present study. Second, as we mention in § 5.2, since the effect of the neighboring arcades cannot be neglected at the third stage, we do not discuss this stage in detail; that is, although it is found that the magnetic island rises at a constant velocity at this stage, it is still an open question whether this constant motion continues all through the third stage. As a matter of fact, looking at Figure 3 carefully tells us that the final rise velocity gradually decreases after $t = 20$, which is unlike the results of our previous study (Magara et al. 1996). In Magara et al. (1996), we studied the reconnection in an antiparallel magnetic-field configuration, where the magnetic island continues to rise at a constant velocity. In our present study, however, the existence of the overlying closed magnetic field exerting the downward force to the magnetic island contributes to the reduction of its rise velocity. In addition, there must be other important effects really working at this stage, such as the effects of the viscosity, the radiative cooling, and crossing other magnetic fields (S. Koutchmy 1996, private communication; C. Delannee 1996, private communication). A study including these effects should be attempted in our future work.

Another uncertainty is the origin of the localization of an initial resistive perturbation. Biskamp & Welter (1989) mentioned the possibility of the resistive structure developing in the arcade center. Priest (1988) suggested that the rising motion of overlying magnetic arcades induced a resistive development beneath it. Wiechen, Büchner, & Otto (1996) studied the nature of the resistive instability developing within a magnetic arcade. They emphasized the importance of the localization of the resistivity. Schumacher & Kliem (1996) showed the dynamical features of the current sheet which is subject to an anomalous kinetic instability.

5.5. *Conclusions*

Considering the results of our present simulation, now we describe how those flares associated with mass eruptions evolve from their preflare phases to gradual phases. We clarify three distinct stages in the evolution, corresponding to the preflare phase, the impulsive or rise phase, and gradual phase, and investigate every stage's dynamical nature in detail. Figure 11 shows the schematic views of the evolution of eruptive flares. In this figure initial resistive instability starts inside the arcade at $t = t_1$, which forms a magnetic island. This magnetic island is ejected upward slowly by the outflow from the neutral point produced by the initial resistive processes. As the magnetic island rises, the gas density decreases and the spatial gradient of the magnetic field increases around the neutral point, which means that the ion-electron drift velocity at the neutral point increases, leading to the occurrence of the anomalous

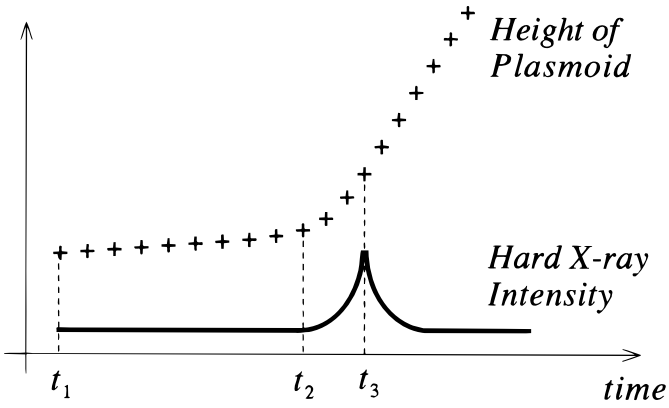

FIG. 11.—Schematic illustration of evolution of an eruptive flare. Crosses and thick curves represent temporal variations both of height of plasmoid and of hard X-ray intensity. At $t = t_1$, initial resistive instability starts inside the arcade, and the plasmoid begins to rise slowly. At $t = t_2$, anomalous resistivity sets in, and the acceleration of plasmoid starts. At $t = t_3$, perpendicular magnetic field around neutral point is lost and hence the rate of magnetic reconnection increases, which implies that hard X-ray intensity reaches its maximum.

resistivity (at $t = t_2$). Then the outflow from the neutral point is rapidly developing, beginning to accelerate the magnetic island (from t_2 to t_3). When the anomalous resistivity sets in, the neutral-point electric field arises, but it does not reach its maximum value as long as a large amount of perpendicular magnetic field exists around the neutral point because of the inhibition of the efficient magnetic reconnection. At $t = t_3$, the neutral-point electric field reaches its maximum, which implies that the high-energy electrons can be generated and high-energy radiation, such as hard X-rays, can be emitted. At that time there occurs the violent energy release causing a reconnection jet which forms the fast MHD shock at the bottom of the magnetic island. After that the O-point (central part of the magnetic island) turns to be behind the shock, and hence strong acceleration no longer occurs.

Since the role of the perpendicular magnetic field in the scenario described above is very important, we will attempt a more detailed study of this property in the future. This kind of study was done by Birn & Hesse (1991), who discussed magnetic reconnections in the Earth's magnetotail and found the concentration of the electric field around an X-point.

6. SUMMARY

Finally, we summarize the main results of our paper as follows:

1. We investigate the plasmoid dynamics in the evolution of eruptive flares. At the first stage, the magnetic island slowly rises by the upflow produced by the initial resistive perturbation and then begins to be accelerated when the anomalous resistivity sets in. This acceleration stops after the fast MHD shock is formed at the bottom of the magnetic island, which implies that the upflow around the central part of the magnetic island is no longer strong. However, it is still an open question whether the magnetic island continues to rise at a constant velocity later.

2. A time lag between the start time of the magnetic island acceleration and the peak time of the neutral-point electric field is explained by the inhibition of the magnetic reconnection by the perpendicular magnetic field, although the detailed process should be studied in the future. This time lag is similar to the observed time lag between the start time of the plasmoid acceleration and the peak time of the hard X-ray intensity (Ohyama & Shibata 1997).

3. Comparing the simulation results with the observational ones, we find that the real rising motion of the plasmoid is quite slower than our simulation. By studying the initially perturbed region, we conjecture that in actual situations, the initial resistive perturbation proceeds very weakly and at many positions inside the arcade.

4. Those models in which the vertical extent of a magnetic arcade is several times larger than its horizontal extent are unstable for resistive perturbations and are expected to cause the anomalous resistivity, leading to the eruptive phenomena. This is consistent with the conclusion of Kusano et al. (1995).

5. We do not show how the localization of an initial resistive perturbation occurs, which will be discussed in our future work.

The authors thank S. Tsuneta, B. Schmieder, S. Koutchmy, and C. Delannee for their useful suggestions. We also appreciate M. Ohyama, M. Shimojo, and the other *Yohkoh* team members providing us with some excellent data. The numerical computations have been carried out using FACOM VPX210/10S at the National Institute of Fusion Science.

REFERENCES

Berman, R. H., Tetreault, D. J., & Dupree, T. H. 1985, Phys. Fluids, 28, 155
Birn, J., & Hesse, M. 1991, J. Geophys. Res., 96, 23
Biskamp, D., & Welter, H. 1989, Sol. Phys., 120, 49
Bogaert, E., & Goossens, M. 1991, Sol. Phys., 133, 281
Borovsky, J. E. 1986, ApJ, 306, 451
Browning, P. K., & Priest, E. R. 1986, A&A, 159, 129
Cargill, P. J., Hood, A. W., & Migliuolo, S. 1986, ApJ, 309, 437
Choe, G. S., & Lee, L. C. 1996, ApJ, 472, 360
Finn, J. M., Guzdar, P. N., & Chen, J. 1992, ApJ, 393, 800
Forbes, T. G. 1990, J. Geophys. Res., 95, A8, 11919
Forbes, T. G., & Priest, E. R. 1983, Sol. Phys., 84, 169
Forbes, T. G., Priest, E. R., & Isenberg, P. A. 1994, Sol. Phys., 150, 245
Hara, H. 1996, Ph.D. thesis, Univ. Tokyo
Heyvaerts, J., & Priest, E. R. 1984, A&A, 137, 63
Hood, A. W., & Anzer, U. 1987, Sol. Phys., 111, 333
Hudson, S. H. 1994, in Proc. Kofu Symp., ed. S. Enome & T. Hirayama (Nagaro: NRO), 1
Inhester, B., Birn, J., & Hesse, M. 1992, Sol. Phys., 138, 257
Kusano, K., Suzuki, Y., & Nishikawa, K. 1995, ApJ, 441, 942
Magara, T., Mineshige, S., Yokoyama, T., & Shibata, K. 1996, ApJ, 466, 1054
Masuda, S. 1994, Ph.D. thesis, Univ. Tokyo
Mikic, Z., Barnes, D. C., & Schnack, D. D. 1988, ApJ, 328, 830
Ohyama, M., & Shibata, K. 1997, PASJ, 49, 249
Ono, Y., Morita, A., & Katsurai, M. 1993, Phys. Fluids B5, 10, 3691
Parker, E. N. 1979, Cosmical Magnetic Fields (Oxford: Oxford Univ. Press)
———. 1994, Spontaneous Current Sheets in Magnetic Fields (Oxford: Oxford Univ. Press)
Platt, U., & Neukirch, T. 1994, Sol. Phys., 153, 287
Priest, E. R. 1982, Solar Magnetohydrodynamics (Dordrecht: Reidel)
———. 1988, ApJ, 328, 848
Priest, E. R., & Forbes, T. G. 1990, Sol. Phys., 126, 319
Sakao, T. 1994, Ph.D. thesis, Univ. Tokyo
Schmieder, B., Démoulin, P., Aulanier, G., & Golub, L. 1996, ApJ, 467, 881
Schumacher, J., & Kliem, B. 1996, Phys. Plasma, 3, 4703
Shibata, K., Tajima, T., Steinolfson, R. S., & Matsumoto, R. 1989, ApJ, 345, 584
Shibata, K., et al. 1994, ApJ, 431, L51
———. 1995, ApJ, 451, L83
Steele, C. D. C., Hood, A. W., Priest, E. R., & Amari, T. 1989, Sol. Phys., 123, 127
Steele, C. D. C., & Priest, E. R. 1989, Sol. Phys., 119, 157
Tsuneta, S. 1996, in Solar and Astrophysical Magnetohydrodynamic Flows, ed. K. C. Tsinganos (Dordrecht: Kluwer), 85
Tsuneta, S., et al. 1992, PASJ, 44, L63
Ugai, M. 1986, Phys. Fluids, 29, 3659
———. 1996, Phys. Plasmas, 3, 4172
van Ballegooijen, A. A., & Martens, P. C. H. 1989, ApJ, 343, 971
van der Linden, R., Goossens, M., & Hood, A. W. 1988, Sol. Phys., 115, 235
Velli, M., & Hood, A. W. 1986, Sol. Phys., 106, 353
Wiechen, H., Büchner, J., & Otto, A. 1996, J. Geophys. Res., 48, 845
Yokoyama, T. 1995, Ph.D. thesis, Graduate Univ. for Advanced Studies (National Astronomical Observatory)
Yokoyama, T., & Shibata, K. 1994, ApJ, 436, L197
Zweibel, E. G. 1981, ApJ, 249, 731
———. 1982, ApJ, 258, L53
Zwingmann, W. 1987, Sol. Phys., 111, 309